nature communications

Article

https://doi.org/10.1038/s41467-025-56394-9

Stepwise amplification of circularly polarized luminescence in indium-based metal halides by regulating their structural dimension

Received: 19 August 2024

Accepted: 17 January 2025

Published online: 10 February 2025

Check for updates

Cui-Mi Shi[1,2,3], Haolin Lu[4], Jin-Yun Wang[1], Guankui Long[4] ✉, Liang-Jin Xu[1,2,3] ✉ & Zhong-Ning Chen[1,2,3]

The pursuit of chiral lead-free metal halides with both high photoluminescence quantum yield (PLQY) and large luminescence dissymmetry factor (g_{lum}) remains a priority for designing efficient circularly polarized light sources. However, a tradeoff exists between PLQY and g_{lum} in chiral materials due to the mismatched electric (**μ**) and magnetic transition dipole moment (**m**). Herein, we address this contradiction and develop the efficient circularly polarized luminescence (CPL) emitters through structural dimension modulation. By tuning the size and polarization of chiral organic cations and employing the cascade cationic insertion strategy, 0D, 1D and 3D indium-based chiral metal halides are constructed. These hybrids exhibit self-trapped excitons emission with near-unity PLQY, while the $|g_{lum}|$ boosts exponentially from 10^{-3} to nearly 10^{-1} as the structural dimension increases from 0D to 3D, and the highest $|g_{lum}|$ of 0.89×10^{-1} has been achieved. Structural analysis and theoretical calculation indicate the increased structural dimension promotes the formation of helical structure and enlarges magnetic transition dipole moment, thus resulting in improved CPL performance. Our research provides valuable insights on the relationship between g_{lum} and structural dimension, thus will advance the development of efficient CPL-active materials for practical applications.

Chiral materials featuring circularly polarized luminescence (CPL) are currently garnering significant attention for their potential applications in 3D displays, quantum computing, spintronic devices, and information storage[1–4]. The luminescence dissymmetry factor, g_{lum}, is a key metric to evaluate CPL performance, which is obtained from Eq. (1):

$$g_{lum} = \frac{2(I_L - I_R)}{I_L + I_R} = \frac{4\mathbf{m}\boldsymbol{\mu}\cos(\theta)}{\mathbf{m}^2 + \boldsymbol{\mu}^2} \quad (1)$$

where I_L and I_R represent the emission intensities of left- and right-handed circularly polarized light, **μ** and **m** are the electric and magnetic transition dipole moment vectors, respectively, and θ is the angle between these two vectors[5,6]. Generally, $|\boldsymbol{\mu}|$ is much larger than $|\mathbf{m}|$, leading to a mismatch between electric and magnetic transition dipole moment, which results the g_{lum} value around 10^{-4} to 10^{-3}. An ideal CPL emitter should have both large g_{lum} and high photoluminescence quantum yield (PLQY), the former represents the polarization purity of the emitted light, while the latter evaluates the effectiveness of energy conversion. In this case, the figure of merit

[1]State Key Laboratory of Structural Chemistry, Fujian Institute of Research on the Structure of Matter, Chinese Academy of Sciences, Fuzhou 350002, China. [2]Fujian Science & Technology Innovation Laboratory for Optoelectronic Information of China, Fuzhou 350108, China. [3]University of Chinese Academy of Sciences, Beijing 100049, China. [4]Tianjin Key Lab for Rare Earth Materials and Applications, School of Materials Science and Engineering, Nankai University, Tianjin 300350, China. ✉e-mail: longgk09@nankai.edu.cn; xuliangjin@fjirsm.ac.cn

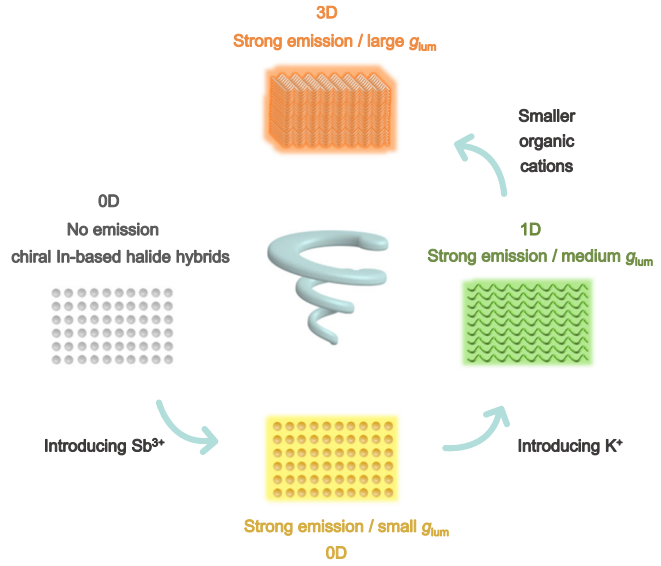

Fig. 1 | CPL performance optimization strategy. Schematic diagram for constructing the chiral metal halide hybrids with different structural dimensions by manipulating chiral organic cations and introducing K^+ and Sb^{3+} ions. The gray represents the hybrid is nonluminous, and yellow, green, and orange-red shadows represent the luminescent colors of corresponding hybrids, respectively.

(FOM) has been proposed to quantify CPL performance and estimate the potential of materials for practical applications, which can be calculated by the product of g_{lum} and PLQY (FOM = g_{lum} × PLQY)[7,8]. The design challenges lie in balancing the g_{lum} and PLQY via modulating both the value and orientation of **μ** and **m**. Numerous researches in this field have already been carried out and a series of excellent CPL-active materials have emerged including chiral organic small molecules[9,10], inorganic nanomaterials[11,12], and metal complexes[13–15]. However, most of them are barely promising for brilliant CPL emitters due to their high cost, poor thermal stability and luminescence intensity. For example, the synthesis of chiral organic molecules or chiral metal complexes is tedious and costly, and they often suffer from poor thermal stability and low luminescence intensity. Inorganic nanomaterials, on the other hand, require coating prefabricated nanomaterials with chiral passivating ligands to achieve CPL, and their properties are challenging to precisely control.

Recently, lead-free metal halide hybrids have become a research hotspot due to their low cost and facile synthesis[16,17], diverse topological structures[18,19], and high PLQY[20,21]. The use of chirality-induced spin selectivity (CISS) effect further endows such materials more stable intrinsic chirality with excellent CPL behavior, positioning them as promising candidates for high-performance CPL emitters[22,23]. The principle involves directly incorporating chiral organic cations into the metal halide lattice, imparting them inherent chirality. The asymmetric hydrogen bonds between chiral organic cations and halide ions often exacerbate lattice distortion, leading to the deformation of excited state. This deformed excited state further induces the generation of self-trapped excitons (STEs), thereby initiating efficient STEs emission and exhibiting chiral luminescent properties. Several significant achievements have been realized in chiral lead-free metal halides[24–34]. For instance, Quan et al. reported a pair of 0D indium-antimony chlorides with near-unity STEs emission and g_{lum} of $\pm1.0\times10^{-2}$[35]. Mao and colleagues realized a g_{lum} of $\pm2.3\times10^{-2}$ in the 1D chiral Mn-based halides (*R*/*S*-3-quinuclidinol)$MnBr_3$ with PLQY of 50.2%[36]. Additionally, Xu et al. reported two CPL-active metal halide enantiomers: 0D (*R*/*S*-$C_6H_{15}ClNO)_2$•$SbCl_5$ ($C_6H_{15}ClNO^+$ = (3-chloro-2-hydroxypropyl) trimethylammonium cation) and 1D (*D*/*L*)-(*tert*-butylprolinate) $MnCl_3$ with the PLQY higher than 70%[37,38]. The g_{lum} for 0D (*R*/*S*-$C_6H_{15}ClNO)_2$•$SbCl_5$ is $\pm3.0\times10^{-4}$, while for 1D (*D*/*L*)-(*tert*-butylprolinate)$MnCl_3$ is $\pm6.0\times10^{-3}$. Recently, Zhang's team reported the best-brightness CPL-active metal halides to date using the cascade cationic insertion strategy with FOM value reaching 2.26×10^{-2} [25]. Despite the progress, the CPL performance implemented above is still not governed by any specific rules and is typically obtained through a trial-and-error approach. Therefore, it is highly needed to clarify the relationship between structures and chiroptical properties in chiral metal halide hybrids and provide effective guidance for designing efficient circularly polarized light sources.

In this work, we develope an efficient strategy to achieve both high PLQY and large g_{lum} in chiral metal halide hybrids by regulating their structural dimensions (Fig. 1). Specifically, the 0D, 1D, and 3D In-based hybrids are rationally designed and constructed by tuning the size and polarization of chiral organic cations with strong hydrogen-bonding-acceptors (oxygen heteroatom), which can coordinate with K^+ ions and enhance the chirality transfer. Bright emission with the near-unity PLQY is obtained in these hybrids. Furthermore, the contradiction between PLQY and g_{lum} is overcame by regulating the structural dimensions which enhances the chiral induction effect and balances the values of electric and magnetic transition dipole moment. As a result, the g_{lum} of these hybrids show an exponential growth from 10^{-3} to nearly 10^{-1} orders of magnitude as the structural dimension increases from 0D to 3D. Both the $|g_{lum}|$ (0.89×10^{-1}) and FOM (0.79×10^{-1}) are the highest values among the reported chiral metal halides to date. Our work elucidates the relationship between structural dimension and g_{lum} in chiral metal halides, and provides a simple pathway for the rational design of efficient CPL-active metal halide hybrids with both high PLQY and large g_{lum}.

Results

Characterizations of *R*/*S*-0DIn

We construct a pair of chiral 0D In-based metal halide hybrids, *R*/*S*-$(MeML)_2InCl_5{\cdot}2H_2O$ (*R*/*S*-0DIn), by self-assembling chiral amine *R*/*S*-MeML and In_2O_3 in hydrochloric acid solution (*R*/*S*-MeML = *R*/*S*-3-methylmorpholine). Single-crystal X-ray diffraction (SCXRD) analyses reveal that *R*-0DIn and *S*-0DIn display a mirrored geometric configuration, and both of them crystallize in the chiral monoclinic space group $P2_1$. In this structure, the In^{3+} ion is coordinated with five Cl^- ions and one water molecule, forming a [$InCl_5(H_2O)$] octahedron. The bulky ammonium cations (*R*/*S*-$MeML^+$) and free water molecules separate adjacent [$InCl_5(H_2O)$] octahedron, resulting in a typical 0D structure at the molecular level (Fig. 2a, Supplementary Fig. 1 and Supplementary Table 1). Their phase purity is confirmed by powder X-ray diffraction (PXRD) patterns (Fig. 2b and Supplementary Fig. 2). The Fourier transform infrared (FT-IR) spectra confirm the introduction of chiral organic cations, as evidenced by distinct characteristic peaks for O-H, N-H, C-H, C-O, and C-N (Supplementary Fig. 3a, b). Additionally, elemental analysis of C, H, and N content in *R*/*S*-0DIn closely aligns with the theoretical content (Supplementary Table 2). The elemental mapping image collected by energy dispersive X-ray spectroscopy (EDS) confirms a homogeneous distribution of In and Cl elements (Supplementary Fig. 4a, b). Subsequently, the photophysical properties are further investigated, revealing a strong absorption peak at 200 nm attributed to the organic ligand, and a weak absorption band in the range of 300–400 nm resulting from the parity-forbidden transition of In^{3+} (Supplementary Fig. 5). Unfortunately, although *R*-0DIn and *S*-0DIn exhibit opposite polarization absorption in the range of 300–700 nm, the negligible photoluminescence (PL) is observed in them, akin to most reported chiral In-based halide hybrids (Fig. 2c)[27].

Characterizations of *R*/*S*-0D

It is well-known that Sb^{3+} doping can greatly enhance the luminous efficiency of In-based hybrids. Then the Sb^{3+}-doped *R*/*S*-$(MeML)_3InCl_6$ (*R*/*S*-$(MeML)_3InCl_6$: Sb^{3+}) have been prepared using a synthesis method

https://doi.org/10.1038/s41467-025-56394-9

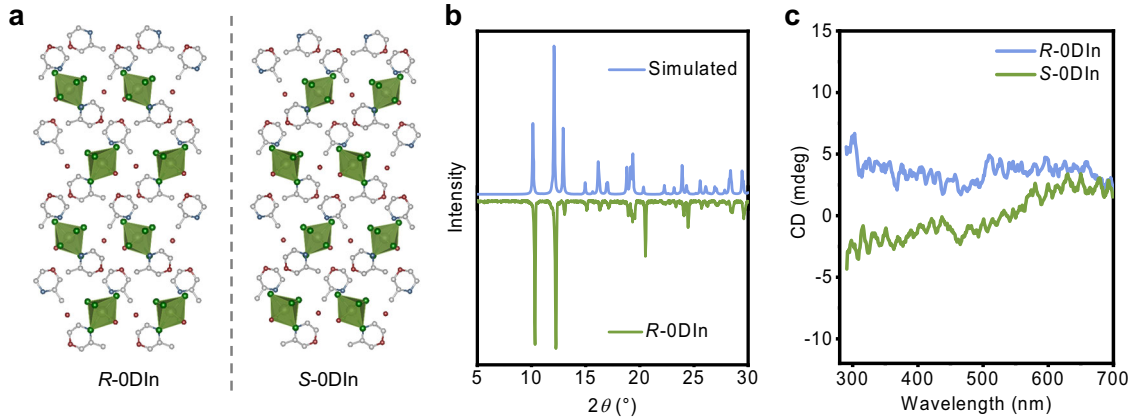

Fig. 2 | Structural analysis and photophysical properties of *R*/*S*-0DIn. a The crystal structures of *R*/*S*-0DIn (In: light green, Cl: dark green, O: red, N: blue, C: grey, and hydrogen atoms are omitted for clarity). **b** The PXRD pattern of *R*-0DIn (green) and the corresponding simulated result (blue) from crystal structure. **c** The circular dichroism (CD) spectra of *R*-0DIn (blue) and *S*-0DIn (green).

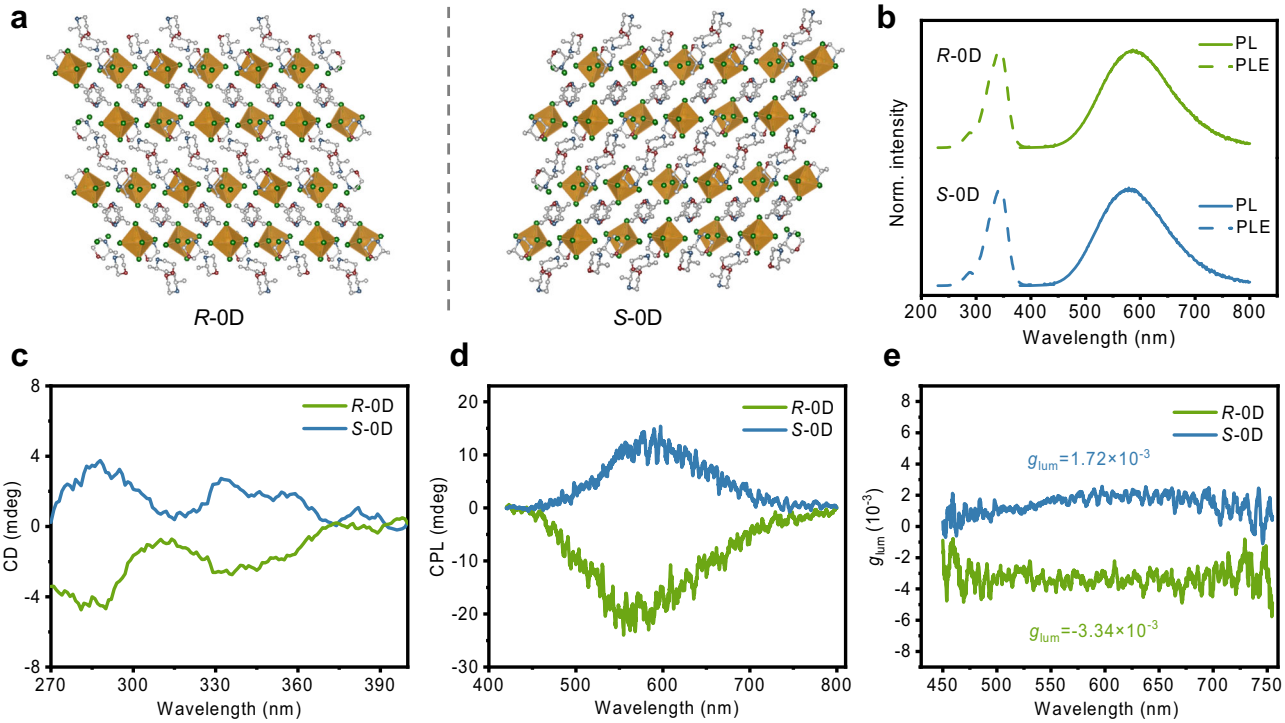

Fig. 3 | Structural analysis and photophysical properties of *R*/*S*-0D. a The crystal structures of *R*/*S*-0D (In or Sb: brown, Cl: dark green, O: red, N: blue, C: grey, and hydrogen atoms are omitted for clarity). **b** The PL (solid line) and PLE (dot line) spectra of *R*-0D (green) and *S*-0D (blue). **c** The CD spectra of *R*-0D (green) and *S*-0D (blue). **d** The CPL spectra of *R*-0D (green) and *S*-0D (blue). **e** The g_{lum} values of *R*-0D (green) and *S*-0D (blue).

similar to that of 0D *R*/*S*-0DIn. The resulting *R*/*S*-(MeML)$_3$InCl$_6$: Sb^{3+} also crystallize in the chiral space group $P2_1$, albeit with slight differences in their coordination modes (Fig. 3a, Supplementary Figs. 6, 7 and Supplementary Table 3). The In^{3+} (or Sb^{3+}) ion is coordinated with six Cl$^-$ ions, forming [In(Sb)Cl$_6$] octahedron. These octahedrons are effectively separated by the bulky organic cations to form a typical 0D structure. The inductively coupled plasma optical emission spectroscopy (ICP-OES) measurements confirm the incorporation of Sb^{3+}, with the actual concentration slightly higher than the feed ratio (Supplementary Table 4). The FT-IR spectra and elemental analysis demonstrate the existence of chiral organic cations (Supplementary Fig. 3c, d and Supplementary Table 2), and the EDS elemental mapping identifies the elements of In, Sb and Cl are uniformly distributed in the crystal (Supplementary Fig. 4c, d).

The photophysical properties are further investigated on the *R* configuration of these metal halides with the Sb^{3+} doping concentration of 0.10 (*R*-0D). This concentration represents the molar ratio Sb/(Sb+In), with 0.10 selected for its optimal luminescence efficiency (Supplementary Fig. 8). As depicted in Supplementary Fig. 9, the metal halide *R*-0D exhibits significant absorption in the range of 280 to 400 nm, corresponding to its photoluminescence excitation (PLE) spectrum. Besides, it exhibits bright yellow emission peaked at 585 nm with PLQY of 83.44% (Fig. 3b, Supplementary Fig. 10). The time-resolved PL decay curve of *R*-0D shows a luminescence lifetime of 5.89 μs with the character of triplet decay, similar to previously reported 0D Sb-based hybrids (Supplementary Fig. 11)[39,40]. Additionally, a large Stokes shift of 242 nm and a full width at half maximum (FWHM) of 147 nm can also be observed.

Table 1 | The summary of photoluminescence efficiency and CPL performance of chiral hybrids

Sample	Dimension	PLQY (%)	g_{lum} (10^{-3})	FOM (10^{-3})
R-0D	0D	83.44	−3.34	−2.79
S-0D	0D	79.24	1.72	1.36
R-1D	1D	97.07	−9.95	−9.66
S-1D	1D	93.48	10.30	9.63
R-3D	3D	84.83	−88.90	−75.41
S-3D	3D	89.42	88.00	78.69

Excitation wavelength-dependent PL spectra demonstrate that *R*-0D keeps the same emission characteristics under different excitations from 260 to 380 nm, confirming the emission originates from the same excited state (Supplementary Fig. 12). The PL and PLE spectra on both powder and bulk crystals are carried out to further understand the luminescence mechanism of these chiral halides. As depicted in the Supplementary Fig. 13a, b, the PL and PLE spectra of *R*/*S*-0D in crystalline and powder states show similar profiles, ruling out the defect induced emission. The broadband emission, large Stokes shift, and greater luminescence decay lifetime are typical features of STEs emission, implying the bright yellow emission of *R*/*S*-0D originates from STEs. More favorable evidence has been obtained through analyzing the relationship between emission intensity and excitation power density. As depicted in Supplementary Fig. 14a, b, the linear relationship between them proves that these emissions are irrelevant to the permanent defects. Otherwise, the PL will be saturated when the traps are filled. Analysis is performed by fitting these data by Eq. (2)[41,42]:

$$I = nL^k \tag{2}$$

where I is the emission peak intensity, L is the excitation power density and n is the fitting parameter. The power exponent k is widely used to determine the luminescence mechanism of semiconductors. Normally, $k = 2$ typically indicates photoluminescence from free carrier recombination; $1 < k < 2$ suggests exciton recombination; and $k < 1$ indicates free-to-bound and donor-acceptor transitions. The k of *R*/*S*-0D are estimated to be 1.02 with intrinsic feature of exciton recombination (Supplementary Fig. 14a, b). Moreover, the temperature-dependent photoluminescence is also recorded to validate the STEs emission. As shown in Supplementary Fig. 15, the emission intensity decreases roughly with temperature increasing from 83 to 363 K due to the enhanced non-radiative recombination. However, it rebounds slightly within the temperature range of 203–263 K. This is reasonable because there is competition between STEs emission and non-radiative recombination induced by exciton-phonon coupling. The intensity of exciton-phonon coupling can be evaluated by the Huang-Rhys factor (S) and phonon frequency $\hbar\omega_{phonon}$ using Eq. (3):

$$\mathrm{FWHM} = 2.36\sqrt{S}\hbar\omega_{phonon}\sqrt{\coth\frac{\hbar\omega_{phonon}}{2k_BT}} \tag{3}$$

where ħ is the Planck constant, k_B is the Boltzmann constant, and the values of S and $\hbar\omega_{phonon}$ are estimated to be 29.87 and 33.66 meV, respectively (Supplementary Fig. 16). These high values of S and $\hbar\omega_{phonon}$ indicate a strong electron-phonon coupling effect in *R*-0D, which facilitates the formation of STEs.

The CD and CPL spectra are conducted on *R*/*S*-0D to understand their chiral characteristics. As shown in Fig. 3c, the CD spectrum of *R*-0D exhibits distinct Cotton effects in the wavelength range of 270 to 400 nm, consistent with its corresponding UV-vis absorption spectrum, indicating the chirality transfer from organic cations to inorganic frameworks since chiral organic cations have almost no CD absorption within the range of 300–400 nm (Supplementary Fig. 17a). When the absolute configuration of the chiral organic cation changes from *R* to *S*, the CD signal reverses. Besides, the CPL spectra based on *R*-0D and *S*-0D polycrystalline powders display mirror-image distributions in the range of 420 to 800 nm, with peak centred at around 585 nm (Fig. 3d), matching with the corresponding PL spectra. This alignment confirms that both CPL and PL originate from the same emission state, namely, the STEs. The g_{lum} at the peak positions for *R*/*S*-0D are -3.34×10^{-3} and 1.72×10^{-3}, respectively (Fig. 3e, Table 1), with their corresponding FOM values of -2.79×10^{-3} and 1.36×10^{-3} (Table 1). The low g_{lum} is reasonable considering the weak chirality induction from organic cations to the inorganic framework in 0D structure (Supplementary Fig. 18). Higher structural dimension may benefit the chirality induction due to dense and more orderly packing of chiral cations.

Characterizations of *R*/*S*-1D and *R*/*S*-3D

Based on the aforementioned assumptions, we endeavored to synthesize higher-dimensional In-based hybrids. Fortunately, 1D *R*/*S*-$(MeML)_2KInCl_6$: 0.10 Sb^{3+} (*R*/*S*-1D) have been synthesized by introducing K^+ ions during the synthesis procedure of *R*/*S*-0D. Moreover, 3D *R*/*S*-$(BLOH)_2KInCl_6$: 0.10 Sb^{3+} (*R*/*S*-3D) is also achieved by replacing the *R*/*S*-$MeML^+$ cation with the smaller cation *R*/*S*-$BLOH^+$ (*R*/*S*-$BLOH^+$ = *R*/*S*-3-hydroxypyrrolidine cation, Supplementary Fig. 19 and Supplementary Table 5). As depicted in Fig. 4a, *R*/*S*-1D crystallize in the chiral orthorhombic $P2_12_12$ space group and display 1D chain structure. Each K^+ ion is coordinated with four Cl^- ions and two organic ligands to form a $[KCl_4O_2]$ octahedral geometry. The In^{3+} (or Sb^{3+}) ion is bonded to six Cl^- ions, forming a $[In(Sb)Cl_6]$ octahedron. These two octahedrons are arranged alternately, forming a 1D edge-sharing chain (Supplementary Fig. 20 and Supplementary Table 6). While *R*/*S*-3D crystallize in the chiral triclinic space group $P1$ and exhibit 3D cage-like structure (Fig. 4b). The K^+ ion is coordinated with five Cl^- ions and two organic ligands, forming a $[KCl_5O_2]$ decahedron. Each $[KCl_5O_2]$ unit bonds with the adjacent $[In(Sb)Cl_6]$ octahedron via face-sharing connection to form an asymmetric dimer unit. These dimer units further assemble into a 3D cage-like structure through corner-sharing interaction (Supplementary Fig. 21 and Supplementary Table 7). *R*/*S*-3D differ from traditional 3D chiral perovskites that are typically stacked through electrostatic interactions or rely on surface passivation with chiral ligands. The inclusion of K^+ ions and organic ligands in coordination may enhance chiral induction and transfer. ICP-OES analyses and EDS elemental mapping demonstrate the insertion and uniformly distributed of Sb^{3+} and K^+ in these In-based halide hybrids, and the actual ratios from ICP-OES of Sb^{3+} are lower than the stoichiometric ratio (Supplementary Table 4 and Supplementary Fig. 4e–h). The presence of organic cations is further demonstrated by FT-IR spectra and elemental analysis (Supplementary Fig. 3e–h and Supplementary Table 2). Additionally, the PXRD patterns of these hybrids closely match with the simulated results from SCXRD, confirming their high crystallinity and phase purity (Supplementary Figs. 22, 23). Moreover, thermal stability of these hybrids is revealed by thermogravimetric analysis (TGA), which shows that the thermal stability is significantly enhanced with the increase of structural dimensions. Specifically, the decomposition of *R*/*S*-0DIn starts from before 100 °C, while the thermal decomposition temperatures for *R*/*S*-1D and *R*/*S*-3D are improved to ≈220 and 250 °C, respectively (Supplementary Fig. 24).

Under UV light illumination, *R*-1D exhibits bright green emission peaking at 525 nm, with a PL lifetime of 2.36 μs and a Stokes shift of 180 nm (Fig. 4c and Supplementary Fig. 25). Moreover, *R*-1D exhibits stronger emission than *R*-0D with a PLQY of 97.07% (Supplementary Fig. 26). This near-unity emission may be attributed to the reduction of non-radiative thermal vibrations in $[In(Sb)Cl_6]$ octahedron with the assistance of K^+ coordination. *R*-3D exhibits bright broad orange-red emission centered at 647 nm with a PLQY of 84.83% and lifetime of

https://doi.org/10.1038/s41467-025-56394-9

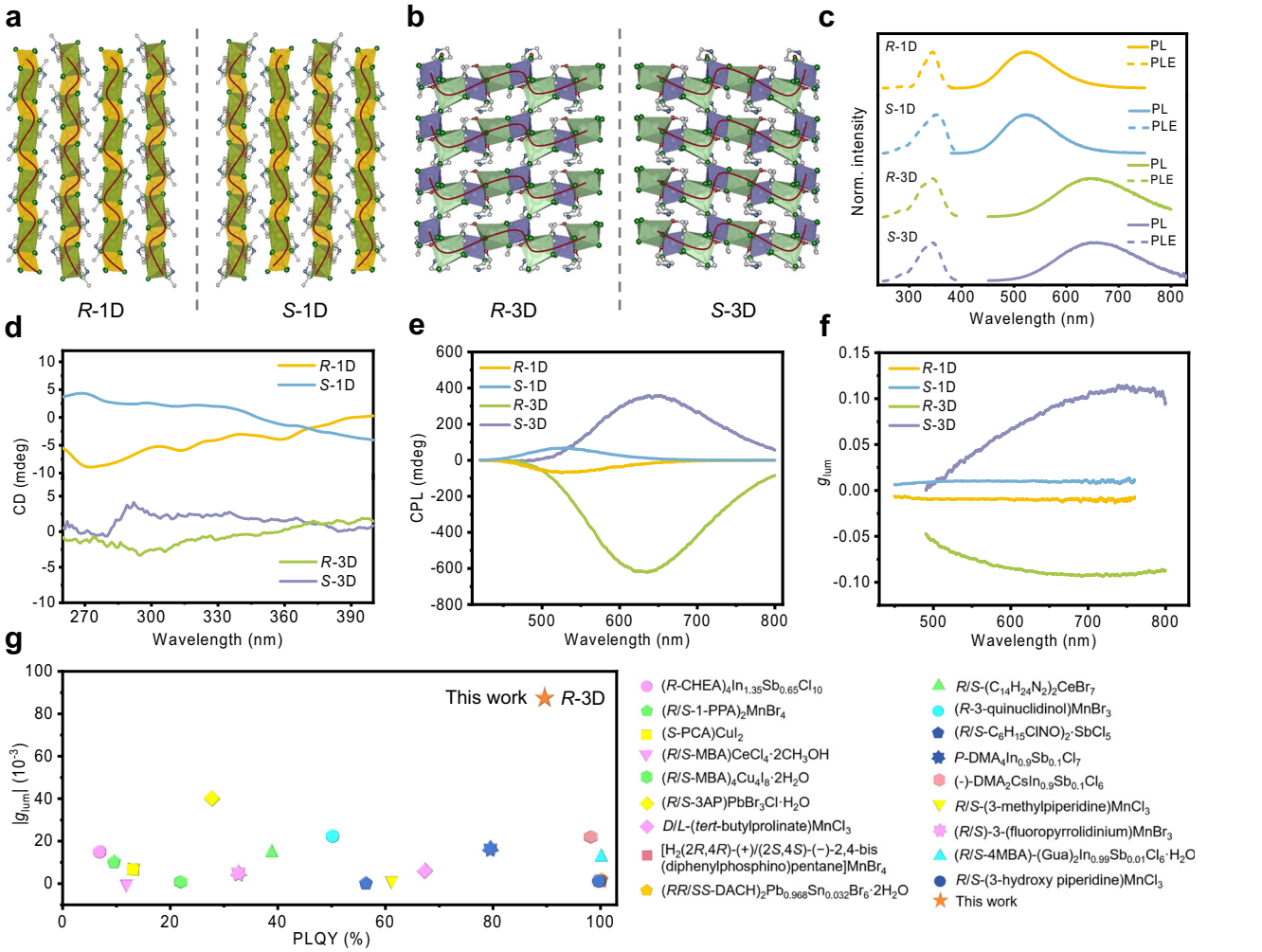

Fig. 4 | Structural analysis and photophysical properties of *R*/*S*-1D and *R*/*S*-3D. **a** The crystal structures of *R*/*S*-1D (In or Sb: yellow, K: light green, Cl: dark green, O: red, N: blue, C: grey, and hydrogen atoms are omitted for clarity). **b** The crystal structures of *R*/*S*-3D (In or Sb: purple, K: light green, Cl: dark green, O: red, N: blue, C: grey, and hydrogen atoms are omitted for clarity). **c** The PL (solid line) and PLE (dot line) spectra of *R*-1D (yellow), *S*-1D (blue), *R*-3D (green) and *S*-3D (purple). **d**, **e**, **f** The CD, CPL spectra and g_{lum} values of *R*-1D (yellow), *S*-1D (blue), *R*-3D (green) and *S*-3D (purple). **g** The comparison of the PLQY and g_{lum} between this work and previously reported results.

6.56 μs (Fig. 4c and Supplementary Figs. 27, 28). The PLQY trend for *R*-0D, *R*-1D and *R*-3D positively correlates with the Sb···Sb distances, consistent with the concentration-quenching effect (Supplementary Fig. 29)[43]. Additionally, the strength of exciton-phonon coupling plays a crucial role, as its enhancement can promote STEs formation and improve PLQY within a certain degree (Supplementary Figs. 16, 30, 31). The emission mechanisms of *R*/*S*-1D and *R*/*S*-3D are likely to derive from STEs, as inferred from the evaluation of the PL and PLE spectra on crystalline and powder states, the excitation wavelength-dependent and temperature-dependent PL spectra, the relationship between the FWHM and temperature, as well as the power-law dependence of the integrated PL intensity of *R*/*S*-1D and *R*/*S*-3D (Supplementary Figs. 13, 14, 30–35). Furthermore, femtosecond transient absorption (TA) measurements reveal a broad photo-induced absorption (PIA) band in the probe region for *R*-1D and *R*-3D (Supplementary Fig. 36), indicating the rapid formation of new electronic states post-photoexcitation, which provides direct evidence for the presence of STEs[44].

Subsequently, the CD and CPL spectra on these 1D and 3D hybrids are also collected to explore the relationship between structural dimension and g_{lum}. As shown in Fig. 4d, both *R*/*S*-1D and *R*/*S*-3D exhibit prominent CD absorption in the range of 260 to 400 nm, aligning well with their UV-vis absorption spectra (Supplementary Figs. 37, 38). Considering chiral organic cations have almost no CD absorption in the range of 300–400 nm, the chirality transfer is proved from organic cations to inorganic framework (Supplementary Fig. 17). In the CPL spectra, *R*-1D and *S*-1D show mirror-image distributions in the range of 420 to 800 nm, with peak centers around 525 nm, consistent with their PL spectra, suggesting that CPL originates from the STEs emission of *R*/*S*-1D (Fig. 4e). The g_{lum} values at the peak positions of *R*-1D and *S*-1D are determined to be -9.95×10^{-3} and 1.03×10^{-2}, respectively, representing a sixfold increase compared to *S*-0D (Fig. 4f, Table 1). And their FOM values are -9.66×10^{-3} and 9.63×10^{-3}, sevenfold than *S*-0D. For *R*-3D and *S*-3D, they also display nearly symmetric CPL signals in the range of 420 to 800 nm, with peak centers around 640 nm (Fig. 4e). Encouragingly, the g_{lum} values measured at the peak positions reach to -0.89×10^{-1} and 0.88×10^{-1} for *R*-3D and *S*-3D, and their FOM are -0.75×10^{-1} and 0.79×10^{-1}, respectively, representing an increase of nearly an order of magnitude compared to *R*/*S*-1D (Fig. 4f, Table 1). We also investigate the PL and CPL performance of metal halide K_3InCl_6: Sb^{3+} without chiral cations. Although it exhibits bright yellow emission, no CPL signal is detected, confirming that the chirality in our materials arises from the chirality-induced effect of the chiral organic cations (Supplementary Figs. 39, 40). To comprehensively demonstrate the influence of structural dimensions on CPL performance, we prepared 0D hybrids (*R*/*S*-BLOH)$_3InCl_6$: Sb^{3+} with *P*1 space group using the same precursors of

https://doi.org/10.1038/s41467-025-56394-9

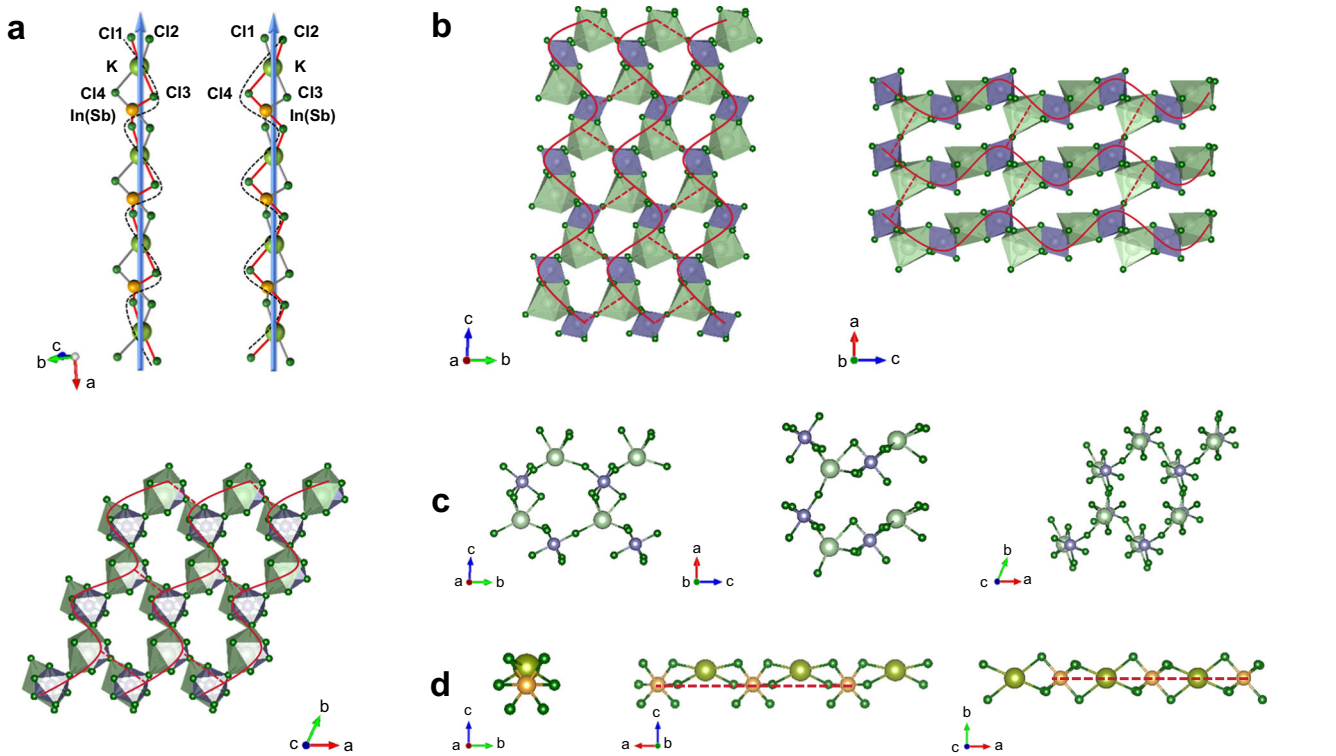

Fig. 5 | Mechanism analysis of the enhanced CPL performance from *R*/*S*-0D to *R*/*S*-1D and *R*/*S*-3D. a The inorganic chain structures of right-handed helix [-KIn(Sb)$Cl_{1,3}$-]$_\infty$ and left-handed helix [-KIn(Sb)$Cl_{2,4}$-]$_\infty$ in *R*-1D (omitting the non-bridging Cl^- ions and organic ligands for clarity). **b** The inorganic skeleton structure of *R*-3D (In or Sb: purple, K: light green, Cl: dark green, and omitting the organic ligands for clarity). The comparison of partial inorganic chain structures in *R*-3D (**c**) and *R*-1D (**d**) from different viewing directions (In or Sb: yellow, K: light green, Cl: dark green for *R*-1D and In or Sb: purple, K: light green, Cl: dark green for *R*-3D, and omitting the organic ligands for clarity).

R/*S*-3D without K^+ ions (Supplementary Fig. 41a). Both hybrids exhibit orange-red emission peaked at around 610 nm, with a PLQY of ≈50% and a PL lifetime of nearly 5.40 µs (Supplementary Fig. 41b–g). Their CPL spectra display mirror-image distributions in the range of 420 to 800 nm, with peak centers around 610 nm, aligning with the corresponding PL spectra (Supplementary Fig. 41h). The g_{lum} values at the peak positions are -2.36×10^{-3} for $(R\text{-BLOH})_3InCl_6$: Sb^{3+} and 2.40×10^{-3} for $(S\text{-BLOH})_3InCl_6$: Sb^{3+}, with their FOM values of -1.25×10^{-3} and 1.18×10^{-3}, respectively (Supplementary Fig. 41i). Clearly, the CPL performance of *R*/*S*-3D with a 3D structure has improved significantly compared to $(R/S\text{-BLOH})_3InCl_6$: Sb^{3+} with a 0D structure. In fact, *R*-3D and *S*-3D present the best circularly polarized luminescence performance in chiral metal halide hybrids to date. Both the FOM (3.5 times higher than the current highest value) and g_{lum} (more than twice the current highest value) are the highest among metal halides with various dimensions (Fig. 4g and Supplementary Table 8)[22,25]. The trend of $|g_{lum}|$ values follow *R*/*S*-3D > *R*/*S*-1D > *R*/*S*-0D, consistent with their structural dimension. Therefore, we speculate that as the structural dimension of metal halide hybrids increases, the interactions between chiral organic ligands and inorganic metal polyhedra become more intimate, favoring the enhancement of chiral induction efficiency and leading to the amplification of g_{lum}.

Analysis of the stepwise amplificated CPL

To support the above speculation, the Hirshfeld surfaces (HS) and fingerprint plots of the organic fractions in *R*-0D, *R*-1D, and *R*-3D are generated using CrystalExplorer to quantify the relative contributions of intermolecular or intramolecular contacts[45]. As shown in Supplementary Fig. 42, the dark red and large circular depressions on the surfaces in *R*-0D, *R*-1D and *R*-3D are assigned to the hydrogen bonds or O···K coordination bonds. In addition, the Hirshfeld 2D-fingerprint plots reveal more detail on interactions. The H···Cl hydrogen bonds are dominant in *R*-0D (34.10%), *R*-1D (41.60%) and *R*-3D (43.70%), which enhance with the increase of structural dimensions. The chiral organic cations with strong hydrogen-bonding-acceptor (oxygen heteroatom) are employed here, which can coordinate with K^+ ions instead of only relying on the electrostatic interactions in most perovskites, resulting in a more stronger chirality transfer. After replacing *R*-$MeML^+$ with the smaller *R*-$BLOH^+$, the contribution of O···K interaction increases from 2.50% to 3.30%. Besides the relative contributions to the Hirshfeld surface area for the contacts between chiral organic fractions and inorganic skeletons (the sum of O···Cl, H···Cl, O···K and H···K) in *R*-0D, *R*-1D and *R*-3D are 34.20%, 46.60% and 49.00%, respectively, demonstrating a more intimate interaction as the structural dimension increases, which favors the enhancement of chirality transfer from chiral organic cations to the inorganic skeletons.

On the other hand, the structural evolution plays an important role in improving the CPL performance as the optoelectronic properties of metal halides are closely tied to their crystal structures. As illustrated in Fig. 4a and Supplementary Fig. 20, the larger $|g_{lum}|$ of *R*-1D compared to *R*-0D can be attributed to the direct connection between chiral ligands and the inorganic skeleton through coordination bonds, whereas *R*-0D only exhibits weak hydrogen bond interactions (Supplementary Fig. 18). *R*-1D achieves intrinsic chirality after self-assembling into helical chiral inorganic chains, where K^+ and In^{3+} (or Sb^{3+}) ions coordinate with Cl_1^- and Cl_3^- to form a right-handed helix [-KIn(Sb)$Cl_{1,3}$-]$_\infty$, and with Cl_2^- and Cl_4^- to produce a left-handed helix [-KIn(Sb)$Cl_{2,4}$-]$_\infty$ (Fig. 5a). Moreover, *R*-3D, with its 3D structure, can be viewed as multiple interconnected 1D chiral chains (Fig. 5b), which will amplify its chiral intensity. Comparing the inorganic chains in *R*-1D and *R*-3D, it is found that In^{3+} (or Sb^{3+}) ions in *R*-3D exhibit slight displacement (Fig. 5c), whereas in *R*-1D, these ions are completely

overlapping (Fig. 5d). Consequently, the $|g_{lum}|$ of *R*-3D is higher than that of *R*-1D. Furthermore, *R*/*S*-3D demonstrate superior CPL performance compared to previously reported 3D chiral metal halides[34], which can be attributed to the presence of a compact helical inorganic framework.

To quantitatively understand the origin of this stepwise amplified g_{lum}, both the **μ** and **m** of these chiral metal halides are estimated based on Eqs. (1), (4).

$$k_r = \frac{\omega^3 n^3 |\boldsymbol{\mu}|^2}{3\pi\varepsilon_0 \hbar c^3} \quad (4)$$

Where k_r is the radiative recombination rate, ω is the frequency of the measured photoluminescence, n is the refractive index of the medium at the monitored frequency, which is set to be 2.29 based on refs. 46,47 ε_0 is the vacuum permittivity and c is the speed of light under vacuum condition. The radiative recombination rate (k_r) and the nonradiative decay rate (k_{nr}) of the monitored PL can be extracted from its PLQY and lifetime (τ), as described by Eqs. (5), (6).

$$\mathrm{PLQY} = \frac{k_r}{k_r + k_{nr}} \quad (5)$$

$$\tau = \frac{1}{k_r + k_{nr}} \quad (6)$$

The electric and magnetic transition dipole moments (**μ** and **m**) of these metal halides are estimated by using the above equations (Eqs. (1), (4)–(6)) and the results are summarized in Supplementary Table 9. Based on Eq. (1), enlarging |**m**| while contracting |**μ**| is critical to achieve a higher g_{lum} (θ is set to be 0 degree in Eq. (1) for convenience)[48]. In our case, The calculated |**μ**| changes slightly, while |**m**| increases significantly from 0.008 μ_B of *R*-0D to 0.035 μ_B of *R*-1D and 0.242 μ_B of *R*-3D, respectively. Therefore, the enlarged |**m**| caused by tuning the structural dimension in chiral metal halides is responsible for this stepwise amplified g_{lum}.

Discussion

In summary, through tuning the size and polarization of A-site cation by employing the cascade cationic insertion strategy, a series of chiral In-based metal halide hybrids with structural dimension ranging from 0D to 1D and 3D are designed and constructed. These hybrids overcome the contradiction between high PLQY and large g_{lum}, and present the best circularly polarized luminescent performance to date. Their $|g_{lum}|$ values show an exponential increase from 1.72×10^{-3} to 0.89×10^{-1} as the structural dimension progresses from 0D to 3D. Structural analysis and theoretical calculation indicate that the formation of chiral helical structure and the enlargement of magnetic transition dipole moment are responsible for this stepwise amplified CPL performance. The implementation of this approach enriches the designing principles of chiral metal halide hybrids, and provides a strategy to construct circularly polarized light sources with both high PLQY and large g_{lum}.

Methods

Materials

Indium oxide (In_2O_3, 99%), antimony trichloride ($SbCl_3$, 99%), (*R*/*S*)-3-methylmorpholine (*R*/*S*-MeML, 97%), (*R*/*S*)-3-hydroxypyrrolidine (*R*/*S*-BLOH, 98%) were purchased from Adamas Reagent Co., Ltd. Potassium chloride (KCl, 99%) and hydrochloric acid (HCl, 38% in water) were purchased from Sinopharm Chemical Reagent Co., Ltd. All reagents and solvents were used without further purification.

Synthesis of *R*/*S*-0DIn

For *R*/*S*-0DIn single crystals, In_2O_3 (0.072 g, 0.26 mmol) and *R*/*S*-MeML (0.158 g, 1.56 mmol) were dissolved in 3 mL of HCl and heated at 100 °C for 1 h until the mixture was completely dissolved. The colorless single crystals were obtained after evaporating for one week at 40 °C.

Synthesis of *R*/*S*-0D

For *R*/*S*-0D, In_2O_3 (0.065 g, 0.23 mmol), $SbCl_3$ (0.012 g, 0.05 mmol) and *R*/*S*-MeML (0.155 g, 1.53 mmol) were dissolved in 3 mL of HCl and heated at 100 °C for 1 h until the mixture was completely dissolved. The colorless single crystals were obtained after evaporating for one week at 40 °C.

Synthesis of *R*/*S*-1D

For *R*/*S*-1D single crystals, In_2O_3 (0.065 g, 0.23 mmol), $SbCl_3$ (0.012 g, 0.05 mmol), KCl (0.038 g, 0.51 mmol) and *R*/*S*-MeML (0.103 g, 1.02 mmol) were put into a 25 mL glass bottle. Subsequently, the mixture was dissolved in HCl completely after heating at 100 °C for 1 h. The colorless crystals were precipitated after volatilization at 40 °C for one week.

Synthesis of *R*/*S*-3D

For *R*/*S*-3D single crystals, In_2O_3 (0.065 g, 0.23 mmol), $SbCl_3$ (0.012 g, 0.05 mmol), KCl (0.038 g, 0.51 mmol) and *R*/*S*-BLOH (0.089 g, 1.02 mmol) were put into a 25 mL glass bottle. Subsequently, the mixture was dissolved in HCl completely after heating at 100 °C for 1 h. The colorless crystals were precipitated after volatilization at 40 °C for one week.

Characterization

SCXRD data were recorded on the Bruker D8 ADVANCE diffractometer with Mo-K_α radiation (λ = 0.71073 Å) and Cu-K_α radiation (λ = 1.54184 Å). The data collection and reduction were carried out using the Bruker APEX3 program for all compounds. All the structures were solved and refined using the SHELXL-97 software package. All non-H atoms were refined anisotropically, and all H atoms placed in idealized positions. PXRD patterns were recorded using Rigaku MiniFlex 600 X-ray diffractometer equipped with a Cu-K_α (λ = 1.54184 Å) radiation in the range of 5–30° at a scan rate of 2.5° min^{-1}. The PL spectra at different temperatures from 83 to 363 K, time-resolved emission data and PLQY were measured on an FLS1000 Edinburgh fluorescence spectrometer equipped with a 450 W xenon lamp or a 150 W microsecond flash lamp as the excitation source. The UV-vis absorption spectra were recorded at room temperature on the PerkinElmer LAMBDA 950 UV-vis spectrophotometer with $BaSO_4$ as the reflectance reference. The ICP-OES measurements were carried out on a HORIBA Jobin Yvon ULTIMA2 instrument. The elemental analysis measurements were conducted on the Vario EL Cube instrument. The scanning electron microscopy and corresponding EDS mapping were performed on a Nova Nano-SEM450 equipment, running at 30 kV and a resolution of 128.9 eV. The CD spectra were acquired using the A Bio-Logic MOS450 CD spectrometer with the scanning rate of 100 nm min^{-1}, and the data interval was 1 nm. The CPL spectra were recorded by the Jasco CPL spectrophotometer (CPL-300). The TGA was measured on a Netzsch STA449F3 from 30 to 800 °C at a ramp rate of 5.00 °C min^{-1} under a nitrogen flux of 100 mL min^{-1}. FT-IR spectra were recorded on Bruker VERTEX 70 FT-IR spectrophotometer with KBr pellets in the range of 4000–400 cm^{-1}. Femtosecond pump-probe TA measurements were performed on a HELIOS (Ultrafast systems) spectrometer using a regeneratively amplified femtosecond CaF_2 crystal laser system (Spitfire Pro-F1KXP, Spectra-Physics; frequency, 1 kHz; max pulse energy, ≈4 mJ; pulse width, 120 fs).

Reporting summary

Further information on research design is available in the Nature Portfolio Reporting Summary linked to this article.

Data availability

The data that support the findings of this study are available from the corresponding authors upon request. X-ray crystallographic structures have been deposited at the Cambridge Crystallographic Data Center (CCDC), under deposition numbers 2364089 (*R*-0DIn), 2364091 (*S*-0DIn), 2364095 (*R*-0D), 2364096 (*S*-0D), 2364090 (*R*-1D), 2364094 (*S*-1D), 2364092 (*R*-3D), 2364093 (*S*-3D).

References

1. Jin, Y., Peng, Q.-C., Xie, J.-W., Li, K. & Zang, S.-Q. Photo-activated circularly polarized luminescence film based on aggregation-induced emission copper(I) cluster-assembled materials. *Angew. Chem. Int. Ed.* **62**, e202301000 (2023).
2. Zhao, T., Han, J., Duan, P. & Liu, M. New perspectives to trigger and modulate circularly polarized luminescence of complex and aggregated systems: energy transfer, photon upconversion, charge transfer, and organic radical. *Acc. Chem. Res.* **53**, 1279–1292 (2020).
3. Long, G. et al. Chiral-perovskite optoelectronics. *Nat. Rev. Mater.* **5**, 423–439 (2020).
4. Long, G. et al. Spin control in reduced-dimensional chiral perovskites. *Nat. Photonics* **12**, 528–533 (2018).
5. Muthig, A. M. T. et al. Mechano-stimulus and environment-dependent circularly polarized TADF in chiral copper(I) complexes and their application in OLEDs. *J. Am. Chem. Soc.* **145**, 4438–4449 (2023).
6. Zhang, Y. et al. Circularly polarized luminescence in chiral materials. *Matter* **5**, 837–875 (2022).
7. Yao, L. et al. Circularly polarized luminescence from chiral tetranuclear copper(I) iodide clusters. *J. Phys. Chem. Lett.* **11**, 1255–1260 (2020).
8. Guo, Q. et al. Multimodal-responsive circularly polarized luminescence security materials. *J. Am. Chem. Soc.* **145**, 4246–4253 (2023).
9. Liao, X.-J. et al. Planar chiral multiple resonance thermally activated delayed fluorescence materials for efficient circularly polarized electroluminescence. *Angew. Chem. Int. Ed.* **62**, e202217045 (2023).
10. Li, H. et al. Stimuli-responsive circularly polarized organic ultralong room temperature phosphorescence. *Angew. Chem. Int. Ed.* **59**, 4756–4762 (2020).
11. Sang, Y., Han, J., Zhao, T., Duan, P. & Liu, M. Circularly polarized luminescence in nanoassemblies: generation, amplification, and application. *Adv. Mater.* **32**, 1900110 (2019).
12. Yang, C.-H. et al. In situ formed perovskite nanocrystal films toward efficient circularly polarized electroluminescence. *Adv. Funct. Mater.* **34**, 2310500 (2024).
13. Luo, P. et al. Highly efficient circularly polarized luminescence from chiral Au_{13} clusters stabilized by enantiopure monodentate NHC ligand. *Angew. Chem. Int. Ed.* **62**, e202219017 (2023).
14. Li, Y.-L. et al. Aggregation induced emission dynamic chiral europium(III) complexes with excellent circularly polarized luminescence and smart sensors. *Nat. Commun.* **15**, 2896 (2024).
15. Willis, O. G., Zinna, F. & Di Bari, L. NIR-circularly polarized luminescence from chiral complexes of lanthanides and d-metals. *Angew. Chem. Int. Ed.* **62**, e202302358 (2023).
16. Bai, W. et al. Ligand engineering enables efficient pure red tin-based perovskite light-emitting diodes. *Angew. Chem. Int. Ed.* **62**, e202312728 (2023).
17. Liu, H. et al. Efficient red light emitting diodes based on a zero-dimensional organic antimony halide hybrid. *Adv. Mater.* **35**, 2209417 (2022).
18. Li, D.-Y. et al. Reversible triple-mode switching in photoluminescence from 0D hybrid antimony halides. *Chem. Mater.* **34**, 6985–6995 (2022).
19. Song, K.-H. et al. Thermochromic phosphors based on one-dimensional ionic copper-iodine chains showing solid-state photoluminescence efficiency exceeding 99%. *Angew. Chem. Int. Ed.* **61**, e202208960 (2022).
20. Luo, J.-B., Wei, J.-H., Zhang, Z.-Z., He, Z.-L. & Kuang, D.-B. A melt-quenched luminescent glass of an organic-inorganic manganese halide as a large-area scintillator for radiation detection. *Angew. Chem. Int. Ed.* **62**, e202216504 (2022).
21. Su, B., Li, M., Song, E. & Xia, Z. Sb^{3+}-doping in cesium zinc halides single crystals enabling high-efficiency near-infrared emission. *Adv. Funct. Mater.* **31**, 2105316 (2021).
22. Li, M. et al. Circularly polarized radioluminescence from chiral perovskite scintillators for improved X-ray imaging. *Angew. Chem. Int. Ed.* **61**, e202208440 (2022).
23. Wei, Y. et al. Circularly polarized luminescence from zero-dimensional hybrid lead-tin bromide with near-unity photoluminescence quantum yield. *Angew. Chem. Int. Ed.* **61**, e202212685 (2022).
24. Ji, X. et al. Chiral 2D Cu(I) halide frameworks. *Chem. Mater.* **34**, 8262–8270 (2022).
25. Song, T. et al. Achieving strong circularly polarized luminescence through cascade cationic insertion in lead-free hybrid metal halides. *Angew. Chem. Int. Ed.* **63**, e202400769 (2024).
26. Wang, B. et al. Environmental-friendly lead-free chiral Mn-based metal halides with efficient circularly polarized photoluminescence at room temperature. *J. Alloys Compd.* **910**, 164892 (2022).
27. Wang, Z. et al. Turn-on circularly polarized luminescence in chiral indium chlorides by $5s^2$ metal centers. *Angew. Chem. Int. Ed.* **62**, e202215206 (2022).
28. Li, J. et al. Circularly polarized luminescence induced by hydrogen-bonding networks in a one-dimensional hybrid manganese(II) chloride. *Angew. Chem. Int. Ed.* **63**, e202405310 (2024).
29. He, X. et al. Bright circularly polarized mechanoluminescence from 0D hybrid manganese halides. *Adv. Mater.* **36**, 2309906 (2024).
30. Li, C. et al. Efficient ultraviolet circularly polarized luminescence in zero-dimensional hybrid cerium bromides. *Angew. Chem. Int. Ed.* **63**, e202403727 (2024).
31. Niu, X. et al. The first chiral cerium halide towards circularly-polarized luminescence in the UV region. *Sci. China Chem.* **67**, 1961–1968 (2024).
32. Song, Z., Yu, B., Liu, G., Meng, L. & Dang, Y. Chiral hybrid copper(I) iodide single crystals enable highly selective ultraviolet-pumped circularly polarized luminescence applications. *J. Phys. Chem. Lett.* **13**, 2567–2575 (2022).
33. Gao, J.-X., Zhang, W.-Y., Wu, Z.-G., Zheng, Y.-X. & Fu, D.-W. Enantiomorphic perovskite ferroelectrics with circularly polarized luminescence. *J. Am. Chem. Soc.* **142**, 4756–4761 (2020).
34. Ji, X. et al. Mono- and bi-dentate chiral ligands lead to efficient circularly polarized luminescence in 0D and 3D semiconducting copper(I) iodides. *Adv. Opt. Mater.* **11**, 2300541 (2023).
35. Liu, Y. et al. Integrating achiral and chiral organic ligands in zero-dimensional hybrid metal halides to boost circularly polarized luminescence. *Angew. Chem. Int. Ed.* **62**, e202306821 (2023).
36. Chen, J. et al. Structural origin of enhanced circularly polarized luminescence in hybrid manganese bromides. *Angew. Chem. Int. Ed.* **61**, e202205906 (2022).
37. Xuan, H.-L., Li, J.-L., Xu, L.-J., Zheng, D.-S. & Chen, Z.-N. Circularly polarized luminescence based on 0D lead-free antimony (III) halide hybrids. *Adv. Opt. Mater.* **10**, 2200591 (2022).
38. Xuan, H.-L. et al. Amino-acid-induced circular polarized luminescence in one-dimensional manganese(II) halide hybrid. *Chem. Eur. J.* **28**, e202201299 (2022).
39. Li, B. et al. Sequential and reversible phase transformations in zero-dimensional organic-inorganic hybrid Sb-based halides towards multiple emissions. *Angew. Chem. Int. Ed.* **61**, e202212741 (2022).

40. Zhang, Z. et al. Crystalline phase recognition induced domino phase transition and luminescence switching for advanced information encryption. *Angew. Chem. Int. Ed.* **60**, 23373–23379 (2021).
41. He, H. et al. Exciton localization in solution-processed organolead trihalide perovskites. *Nat. Commun.* **7**, 10896 (2016).
42. Zhang, T. et al. Regulation of the luminescence mechanism of two-dimensional tin halide perovskites. *Nat. Commun.* **13**, 60 (2022).
43. Zhang, Z.-Z. et al. Co-luminescence in a zero-dimensional organic-inorganic hybrid antimony halide with multiple coordination units. *Dalton Trans.* **50**, 3586–3592 (2021).
44. Wei, J.-H., Luo, J.-B., Liao, J.-F., Ou, W.-T. & Kuang, D.-B. Te^{4+}-doped $Cs_2InCl_5{\cdot}H_2O$ single crystals for remote optical thermometry. *Sci. China Mater.* **65**, 764–772 (2021).
45. Spackman, M. A. & Jayatilaka, D. Hirshfeld surface analysis. *CrystEngComm* **11**, 19–32 (2009).
46. Di Nuzzo, D. et al. Circularly polarized photoluminescence from chiral perovskite thin films at room temperature. *ACS Nano* **14**, 7610–7616 (2020).
47. Lin, J.-T. et al. Tuning the circular dichroism and circular polarized luminescence intensities of chiral 2D hybrid organic-inorganic perovskites through halogenation of the organic ions. *Angew. Chem. Int. Ed.* **60**, 21434–21440 (2021).
48. Liu, Y., Ma, Z., Wang, Z. & Jiang, W. Boosting circularly polarized luminescence performance by a double p-helix and hetero-annulation. *J. Am. Chem. Soc.* **144**, 11397–11404 (2022).

Acknowledgements

This work was supported by the National Natural Science Foundation of China (Grants 22175181, 92061202, U22A20387, 92256202, 52473305, and 12261131500) and the Fujian Science and Technology Project (Grant 2020L3022).

Author contributions

C.S. synthesized, characterized and analyzed data for all chiral hybrids. H.L. and J.W. provided the theoretical calculation support. L.X. conceived the idea of this work and wrote the manuscript. L.X., G.L. and Z.C. supervised and revised the manuscript. All authors discussed the results and commented on the manuscript.

Competing interests

The authors declare no competing interests.

Additional information

Supplementary information The online version contains supplementary material available at https://doi.org/10.1038/s41467-025-56394-9.

Correspondence and requests for materials should be addressed to Guankui Long or Liang-Jin Xu.

Peer review information *Nature Communications* thanks Taotao Zhuang, and the other, anonymous, reviewer(s) for their contribution to the peer review of this work. A peer review file is available.